A Topological Directional Coupler Fed by Microstrip Line With Configurable Coupling Coefficient

Hongyu Shi , *Member, IEEE*, Bolin Li, Luyi Wang , *Graduate Student Member, IEEE*,
Wei E. I. Sha , *Senior Member, IEEE*, Zhihao Lan, Fei Gao , Jianjia Yi, Anxue Zhang , and Zhuo Xu

Abstract—Topological waveguides have been extensively studied for their robust transmission properties immune to defects and their application potentials for microwave and terahertz integrated circuits. In this article, by using grounded planar valley-Hall photonic topological insulators, a high-efficiency topological directional coupler fed directly by microstrip line with configurable coupling coefficient is theoretically proposed and experimentally demonstrated. The topological directional coupler consists of two coupled topological waveguides, which can be directly integrated with microstrip circuits. Different coupling coefficients were achieved by configuring the coupling between the two topological waveguides. Both simulation and measurement demonstrated the proposed designs. In addition, the proposed design is applicable in both microwave and terahertz bands.

Index Terms—Directional coupler, metasurface, planar photonic topological insulators.

I. INTRODUCTION

PHOTONIC topological insulators (PTIs) have great potential to be used as a new type of planar transmission lines with robust edge state transmission, which is compatible with integrated microwave or terahertz (THz) circuits [1], [2], [3], [4], [5], [6]. Different types of planar topological waveguides have been designed based on the spin-Hall PTIs [7], [8], [9], [10], [11], [12] and valley-Hall PTIs [13], [14], [15], [16] from microwave to terahertz band. According to the bulk-edge correspondence principle, the topological waveguides are characterized by their unique electromagnetic (EM) edge modes that are robust against local defects or sharp edges. In addition, unidirectional transport

Hongyu Shi, Bolin Li, Luyi Wang, and Zhuo Xu are with the MOE Key Laboratory for Multifunctional Materials and Structures, Xi'an Jiaotong University, Xi'an 710049, China (e-mail: hongyushi@xjtu.edu.cn; bll506856147@stu.xjtu .edu.cn; bigcrash@stu.xjtu.edu.cn; xuzhuo@mail.xjtu.edu.cn).

Wei E. I. Sha and Fei Gao are with the State Key Laboratory of Modern Optical Instrumentation, College of Information Science and Electronic Engineering, Zhejiang University, Hangzhou 310027, China (e-mail: weisha@zju.edu.cn; gaofeizju@zju.edu.cn).

Zhihao Lan is with the Department of Electronic and Electrical Engineering, University College London, WC1E 6BT London, U.K. (e-mail: z.lan@ee.ucl.ac.uk).

Jianjia Yi and Anxue Zhang are with the School of Information and Communications Engineering, Xi'an Jiaotong University, Xi'an 710049, China (e-mail: jianjia.yi@mail.xjtu.edu.cn; anxuezhang@mail.xjtu.edu.cn).

Color versions of one or more figures in this article are available at https://doi.org/10.1109/JLT.2023.3288342.

Digital Object Identifier 10.1109/JLT.2023.3288342

of EM waves exploiting the effect of pseudospin or valley momentum locking has been realized [17], [18], [19], [20], [21], where chiral sources carrying phase vortices could be utilized to excite these unidirectional EM waves. Nonetheless, engineering applications of topological waveguides are being limited by their mismatch to classical transmission line systems including microstrip lines or coplanar waveguides.

To bridge the gap between classical and topological EM structures, classical-to-topological feeding designs have attracted great attentions. Especially, great efforts have been made to realize topological waveguides that connect to classical transmission line systems with acceptable reflection loss, such as silicon dielectric waveguides [22], [23], antipodal slot lines [24] and rectangular/circular waveguides [3], [4], [25]. High efficiency coupling between silicon photonic waveguide and topological interface was achieved using intermediate refractive index structure with improved field compatibility [22]. Though topological waveguides fed by microstrip lines have been discussed in [24], the design is based on the quantum spin Hall effect and needs two complementary metallic metasurfaces, bringing inconvenience for integration with grounded microstrip line. Therefore, topological waveguides and devices directly compatible with the widely used microstrip line based integrated circuits are still worth exploring, which is particularly useful for on-chip microstrip circuits and antennas [16], [17], [26].

To apply topological waveguides for acoustic or electromagnetic engineering, several topological functional devices were proposed [4], [23], [24], [25], [27]. A topological photonic routing based on the unidirectional excitation of valley-chirality-locked edge states was proposed with a dielectric waveguide feeding [23]. A topological power divider has been realized by introducing a line-defect to silicon valley-Hall photonic crystals at terahertz bands [4]. This design was efficiently excited by a rectangular waveguide with a dielectric tapered coupler. In addition, a hybrid directional/contradirectional topological coupler with a circular waveguide launcher was designed to achieve beam split, cross state and contradirectional coupling in different frequency bands [25]. However, these designs are not compatible to the planar transmission line systems. Recently, a topological coupler fed by an antipodal slot line was designed, and an exponential taper is used to produce gradient momentum between microstrip line and antipodal mode [24]. A -11 dB coupling coefficient for the side channel and a -30 dB isolation for the forward channel were achieved. However, the coupling coefficient is still needed to be improved and made tunable

for more practical applications. Thus, a topological directional coupler with configurable coupling coefficient is still in great desire for antenna array feedings and signal monitoring, et al.

In this article, topological directional couplers directly fed by microstrip lines with high coupling coefficient are designed based on grounded planar valley PTIs with C3 symmetric unit cells, which are also playing critical roles in designing metasurface-based THz emitters [28], generating toroidal pulses of light [29] and realizing vacuum ultraviolet metalens [30]. The design is physically based on quantum valley Hall effect, which only needs one Dirac cone at K/K', requiring only one patterned metallic metasurface whereas the other side of the dielectric could be a fully metalized ground, thus more compatible with the metal background of the microstrip line. Then, based on the above physics, to achieve a mode match to the widely used microstrip lines, a grounded single layer topological structure realization with hexagonal patch and mesh lines was realized to obtain edge states with electric fields compatible to quasi-TEM mode of microstrip line. The topological directional couplers are constructed by two coupled topological valley waveguides and can realize efficient coupling without additional phase modulation. In addition, the coupling coefficient can be configured by tuning the relative geometry between these two topological waveguides, which further widens the potential applications of the proposed design. The designed topological directional couplers were simulated at both microwave and terahertz bands. Samples at microwave band were fabricated and measured. The experimental measurements agree well with the simulation results, which verifies the proposed design.

II. DESIGN PRINCIPLE OF A MICROSTRIP LINE FED TOPOLOGICAL WAVEGUIDE

The grounded planar valley PTI is shown in Fig. 1(a) which consists of hexagonal metal patches connected by metal mesh lines printed on a dielectric substrate with metal ground. The planar refers to the relative low profile (0.029λ at working frequency) of the designed structure. The dielectric substrate is Rogers RO3006 with a relative permittivity $\varepsilon = 6.5$ and a loss tangent $\tan\delta$ of 0.002. The height (h) of the dielectric substrate is 0.625 mm. Each unit cell of the valley PTI is a regular hexagon with side length a of 5.6 mm that consists of a hexagonal metal patch and six metal mesh lines with width $w = 0.1a$. The thickness of the printed metal is 0.035 mm. The hexagonal metal patch is C3 symmetrical and has sides of two different lengths $l1 = a$ and $l2 = 0.5a$. The Δl is defined as $l1 - l2$.

Fig. 1(b) and (c) show the band structure of the planar valley PTI with C6 and C3 symmetry, respectively. The band structure of the valley PTI with C6 symmetry ($l1 = l2$) shows a pair of degenerate Dirac points at the K and K' valleys around 13.7 GHz, which are protected by the time reversal symmetry and inversion symmetry. Introducing C3 structure into each unit cell will break the inversion symmetry and result in the gapping out of the Dirac points, thereby opening a bandgap near the Dirac frequency. Rotating the C3 structure, the bandwidth of the bandgap is
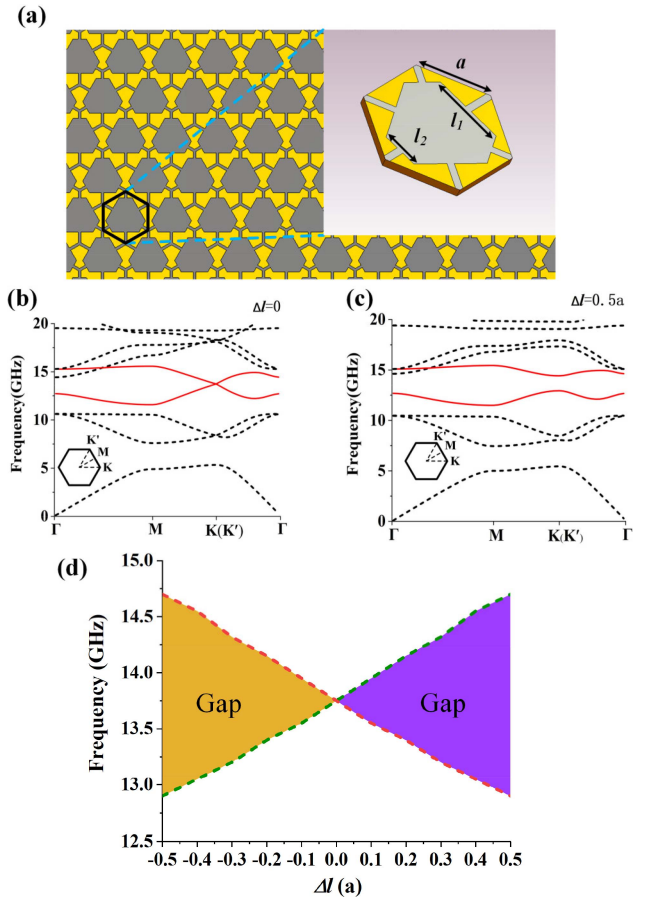

Fig. 1. Geometry and band structure of the planar valley PTIs. (a) Top view of the valley PTI, where the black hexagon shows the unit cell of the valley PTI. (b) Band diagram of the valley PTI with C6 symmetry. (c) Band diagram of the valley PTI with C3 symmetry. (d) Relationship between Δl and the bandgap.

controllable. Similar implementation has also been adopted in [15] and a general discussion of this mechanism can be found in [31]. Therefore, when C6 symmetry is broken to C3 symmetry, the Dirac cones disappear and a bandgap is opened up from 12.9 GHz to 14.4 GHz as shown in Fig. 1(c). The size of the bandgap as a function of Δl presented in Fig. 1(d) shows that in general, when Δl increases from negative to positive value, the valley gap closes and reopens, indicating a band inversion. Moreover, the bigger the $|\Delta l|$ is, the wider the bandgap becomes [3]. This property can be used to control the working bandwidth of the couplers discussed below.

The valley Chern numbers of $C_{K,K'} = 1/2$ are obtained from the integration of the Berry curvature around the two valleys of K and K' [16], [17]. According to the bulk-edge correspondence, the topological valley edge states can be supported in a topological waveguide formed at the interface between two valley PTIs with opposite valley Chern numbers [3], [18]. In Fig. 2(a), we design two types (A-B and B-A type) of domain walls between two planar PTIs and analyze their band structures (Fig. 2(b)) by sweeping k_x from $-\pi/a$ to π/a of the supercell. The valley Chern numbers across the domain walls at K and K' are ± 1. As a result, we can observe A-B type and B-A type valley-Hall edge states (the red line and the blue line) in the band
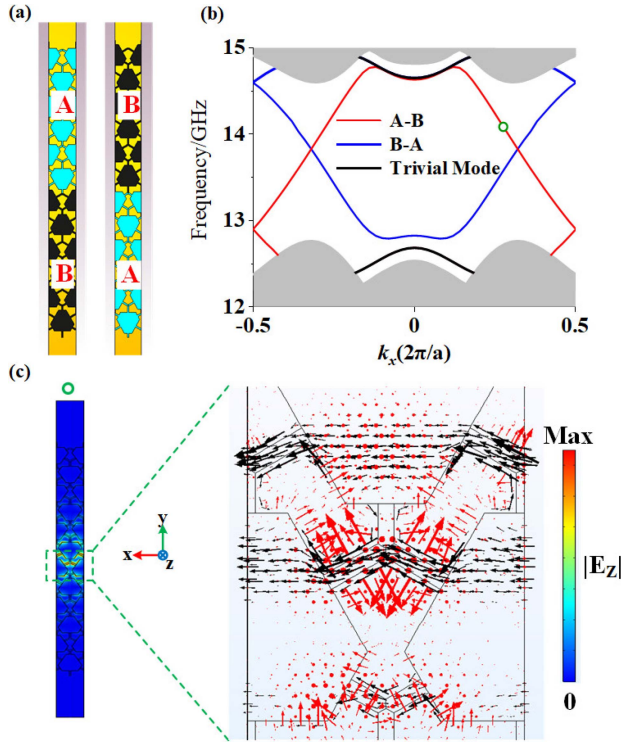
Fig. 2. Design of planar valley PTI waveguides. (a) Supercells of the A-B type (right) and B-A type (left) planar valley PTI waveguides. (b) Band structure of the two supercells. (c) The distribution of the electric field and poynting vectors of the edge state marked by the green circle in (b), where the red arrows represent the direction of the electric field; the red dots are the electric field with only z-direction component and the black arrows represent the poynting vectors. Both the front and the end of the red arrows are located at the metal ground or metal mesh patterns. The metal ground is at z = 0, whereas the metal patches are at z = 0.625 mm.
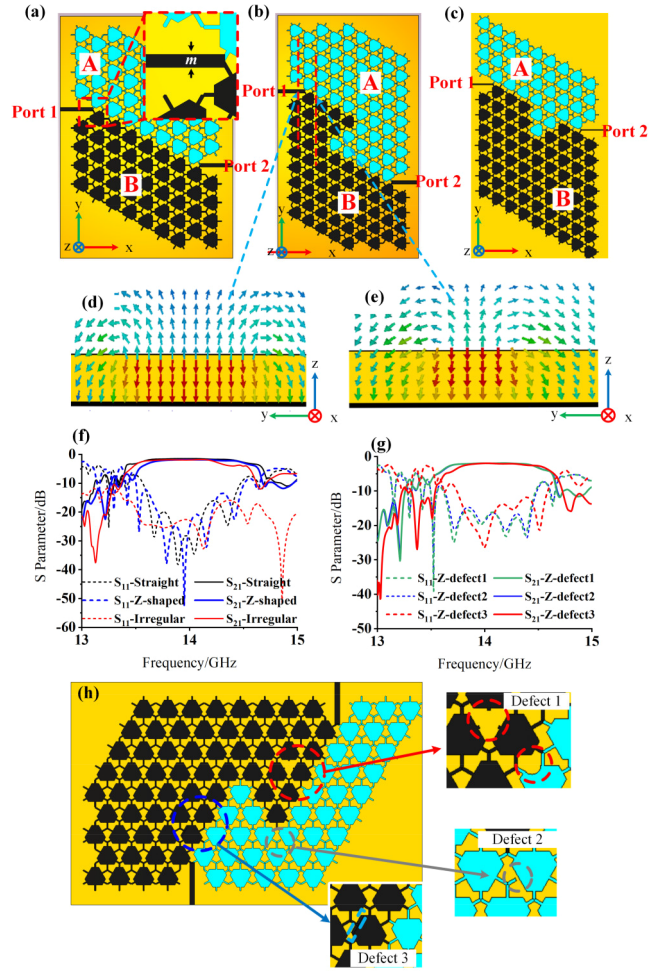

Fig. 3. Planar valley PTI waveguides and simulated transmission results. (a) Straight planar valley PTI waveguide, where the red dotted box is an enlarged view of the feeding structure. (b) Z-shaped planar valley PTI waveguide. (c) Irregular shaped planar valley PTI waveguide. (d) and (e) Electric field distributions in the y-z section of the microstrip feed line and topological waveguide, respectively. (f) Simulated transmission results of the planar valley PTI waveguides. (g) Simulated transmission results of the planar valley PTI waveguides under three defected cases. (h) Z-shaped defected and disordered waveguide with three defected cases.

gap respectively, and they have opposite propagation directions at the K and K' valleys, giving rise to valley-momentum locking. The trivial modes around $k_x = 0$ are given in the black line. In addition, the valley modes connect either to the up (blue) or bottom (red) of the bulk band but not to both. Fig. 2(c) shows the eigenmode viewed from the top of an A-B type edge state marked by the green circle in Fig. 2(b). The electric field of the edge state shows surface wave nature, which is confined near the domain wall and exhibits fast decay vertically away from the domain wall. Moreover, the electric field also concentrates near the metal mesh lines and is orthogonal to the wave propagation direction, which is similar to that in microstrip lines and thus provides a unique opportunity for interfacing with conventional microstrip lines.

To demonstrate this, we construct a straight topological waveguide and a Z-shaped topological waveguide with two 60° bends that both have a zero radius of curvature as shown in Fig. 3(a) and (b), respectively, where a microstrip transmission line with a width of $m = 1.9$ mm is connected to the metal mesh lines to excite the topological waveguides, indicating the A-B type waveguide is compatible with microstrip line of characteristic impedance of 32Ω at 14 GHz. An irregular shaped waveguide is also studied in Fig. 3(c) to demonstrate the robustness of the transmission performance.

The topological waveguides are simulated by the time-domain solver of CST Microwave Studio with the simulation results shown in Fig. 3(f), from which one can see that these topological waveguides can be efficiently fed by microstrip transmission lines with a transmission coefficient (S_{21}) of −1.3 dB and a reflection coefficient (S_{11}) below −10 dB from 13.5 GHz to 14.5 GHz covering almost the bandgap in Fig. 1(c). However, in the real finite sample, there is a slightly frequency shift. In addition, all three waveguides perform similarly, which demonstrates the topological protection of the edge state transmission and generality of the microstrip line feeding technique. The Z-shaped topological waveguides with defects and disorder as shown in Fig. 3(h) are also studied. In Fig. 3(h), the red-circled area (Defect 1) contains defects which affect the hexagon patch and the mesh lines close to the waveguides interface, the grey-circled area (Defect 2) contains defects which affect the mesh lines, the blue-circled area (Defect 3) contains disorder with altered
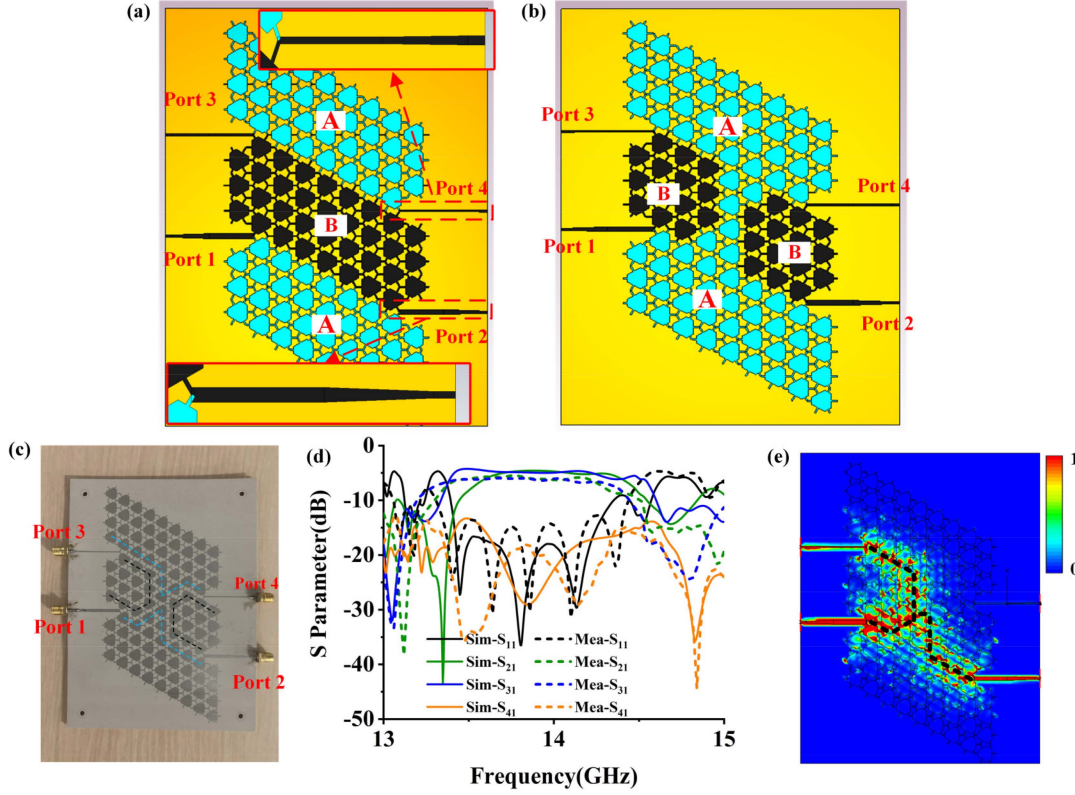
Fig. 4. Design of topological directional couplers. (a) Schematic of a topological directional coupler. The tapered microstrip line is enlarged in the red rectangle. The tapering structure for port 1 and port 2 is identical but different to the tapering for port 3 and port 4. (b) Schematic of an equal-power topological directional coupler. (c) Fabricated prototype of the equal-power topological directional coupler. (d) Simulation and measurement results of the equal-power topological directional coupler. (e) Simulated near-field distribution of the equal-power topological directional coupler. The black dashed line indicates the A-B/B-A type interfaces.

patch size (deviated 20% from the standard size). These defects and disorders (Defect 1, 2 and 3) are shown in one figure for convenience and they are separately simulated. In Fig. 3(g) the S-parameters of the defected Z-shaped waveguide under three cases (Defect 1, 2 and 3) are given. Such three cases are representative scenarios of defects and disorder during manufacturing, and they show similar performance compared with the ideal model, which demonstrates the robustness of the propagation against these defects and disorder. Such robustness is due to the binary valley degree of freedom the waveguide modes carrying, which are separated by a large momentum different in the Brillouin zone. So, if the added defects and disorder are not so strong that they can provide the momentum difference for the inter-valley scattering to happen, this robustness will always persist. In fact, the valley gap in Fig. 2(b) has a sizeable width and the valley edge modes cover almost the whole bandgap. Therefore, we can expect that even if more defects are introduced to the device, as long as the introduced defects are not so strong that they destroy the valley gap and thus the topological protection, the performance of the device will not be severely affected.

To further understand the matching mechanism, the electric field distributions viewed from the side in the y-z plane of the microstrip feed line and grounded topological waveguide are shown in Fig. 3(d) and (e), respectively. The electric field distributions represented by the arrows in Fig. 3(d) and (e) are

demonstrate the high similarity of the propagation modes in microstrip lines and edge state transmission in topological waveguide, which is consistent with the supercell results of A-B-type topological waveguide in Fig. 2(c) and fulfills the spatial mode matching condition. In addition, the characteristic impedance of the topological waveguide is close to the microstrip line due to their similar spatial modes. Further impedance and momentum matching between the 50Ω microstrip line and the topological waveguide is achieved by the tapering of the microstrip line, ensuring the high efficiency of transmission.

III. DESIGN OF A TOPOLOGICAL COUPLER WITH CONFIGURABLE COUPLING COEFFICIENT

A. Equal Power Coupler

The propagation of topological edge states in the topological waveguide exhibits valley-momentum locking behavior, which is essential to construct topological directional couplers. A four-port topological coupler of A-B-A type hetero structure is shown in Fig. 4(a). It can be seen that the coupler is actually a combination of two waveguides consisting of an A-B type (top) and a B-A type (bottom) topological waveguide. The tapered microstrip line is enlarged in the red rectangle. Since A-B and B-A type waveguides have different characteristic impedance and are best fed by microstrip with characteristic impedance of 32 Ω and 60 Ω at 14 GHz, the tapering structure for Port 1 and

Port 2 is identical but different to the tapering for Port 3 and Port 4 for their respective 50 Ω matching. By changing a part of the B-type patterns between the two topological waveguides to A-type patterns, the geometric configurations and spacings of the two topological waveguides can be modified, which provides a flexible way to adjust the coupling strength and the output power of the ports. In all simulations and measurements of the coupler presented below, we fix the port 1 as the input port, and the forward port 2 as the pass-through port. Due to the valley-momentum locking nature of the topological waveguides, port 3 is the coupled port, whereas port 4 behaves as an isolated port. The coupling coefficients of the topological directional couplers could be calculated by the following formula,

$$C = 10 \lg \frac{P_1}{P_3} \qquad (1)$$

where P_1 is the input power of port 1 and P_3 is the output power of port 3.

Generally, in an equal-power splitting system, a completely symmetrical structure plays a very critical role, and when the equal-power output port is not the forward port, the structural design becomes more complicated. As shown in Fig. 4(b), we replace several B-type patterns in Fig. 4(a) by the A-type patterns, so that symmetry of the two topological waveguides is almost preserved. Fabricated prototype of the equal-power topological directional coupler is shown in Fig. 4(c). The simulation and measured results are shown in Fig. 4(d), where the working bandwidth of the equal-power topological coupler is slightly narrower than that of the topological waveguides as shown in Fig. 3(e). As expected, little energy flows out of port 4 (i.e., the isolated port), whereas ports 2 and 3 essentially achieve equal power distribution with the coupling coefficient of $C = -5$ dB. The near-field distribution of the equal-power coupler shown in Fig. 4(e) also demonstrated the valley-Hall topological state and the coupling status between ports. It is also observable that the field distributions are confined mostly in only one period of unit cells along the topological edge with limited edge mode leakage. Therefore, when determining the optimal number of periods of unit cells in the waveguides for their effective operation, one should allow enough number of periods so that there is negligible field distribution at the outmost part.

B. Unequal Power Coupler

Taking the equal-power coupler as a reference, the design of topological directional couplers with configurable coupling coefficient can be realized simply by unit-cell replacement. Specifically, the coupling strength can be enhanced by connecting the two waveguides (see Fig. 5(a)), and conversely, the coupling strength can be reduced by cutting the top and bottom waveguides (see Fig. 5(b)). In addition, since the topological waveguides are robust, no matter how the waveguide shapes are changed, the transmission performances of the topological waveguides will not be affected, which offers a great flexibility to tune the coupling strength of the topological coupler. We design two topological directional couplers with the coupling coefficients of $C = -3.5$ dB and $C = -7$ dB in Fig. 5(a) and (b),
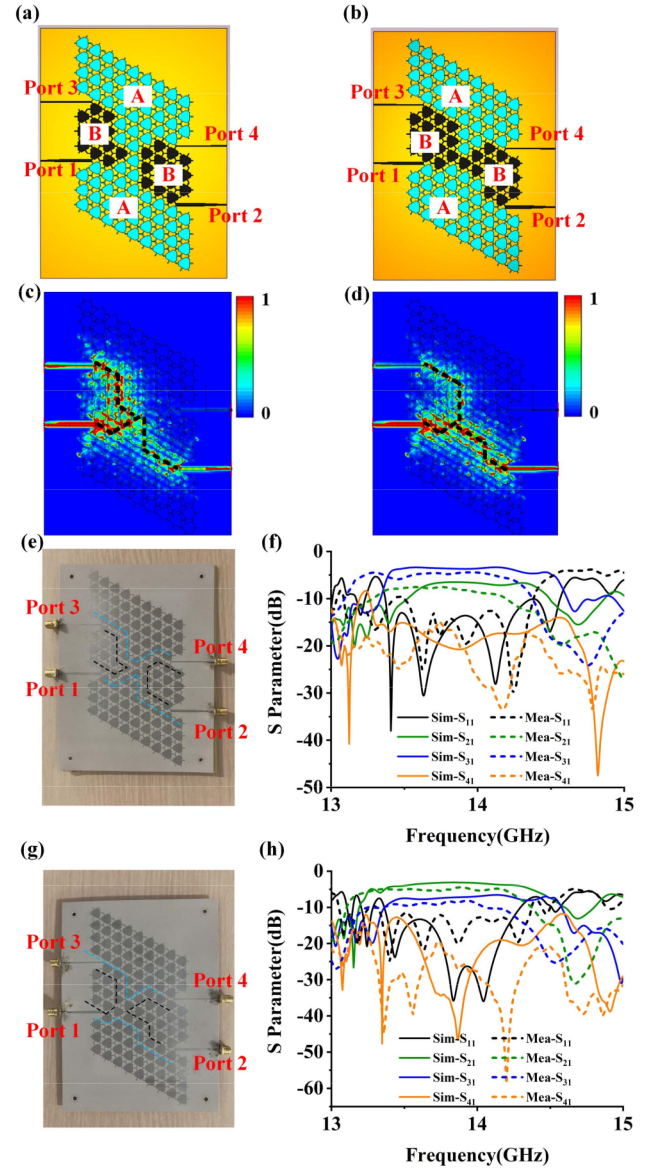

Fig. 5. Unequal power topological directional couplers. (a) And (b) topological directional coupler with the coupling coefficient of $C = -3.5$ dB and $C = -7$ dB. (c) And (d) simulated near-field distribution of the topological directional coupler with the coupling coefficient of $C = -3.5$ dB and $C = -7$ dB. The black dashed line indicates the A-B/B-A type interfaces. (e) And (g) fabricated prototype of unequal power coupler with the coupling coefficient of $C = -3.5$ dB and $C = -7$ dB, respectively. (f) And (h) simulation and measurement results of the unequal power topological directional couplers with the coupling coefficient of $C = -3.5$ dB and $C = -7$ dB.

respectively, and the prototypes are given in Fig. 5(e) and (g). The simulation and measured results are shown in Fig. 5(f) and (h), which demonstrate the configurability of the coupling strength of our proposed topological directional coupler. The near-field distributions are shown in Fig. 5(c) and (d) respectively.

We would like to mention that in the experiments of topological directional couplers, due to the low mechanical strength of the dielectric material used, even if the system is fixed on a rigid sheet, there are still some bendings that cause the unevenness of the board surface which reaches around several millimeters at one side of the substrate. While topological waveguides usually
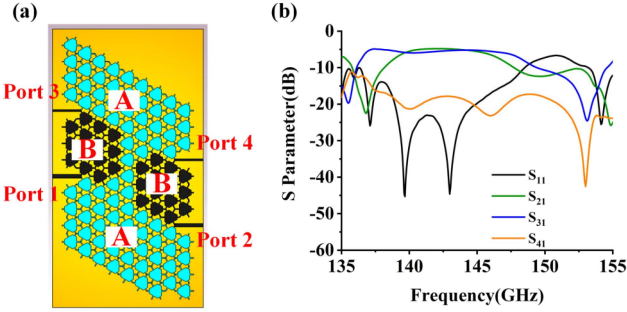
Fig. 6. Design of a THz topological directional coupler with equal-power division. (a) Top view of the THz topological directional coupler. (b) Simulation results of the THz equal power topological directional coupler.

are robust against local defects and disorders, the bending of the board surface as a whole extends a wider range beyond the local regimes, which indeed has a small effect as we found in the experiments. Considering relative dimension with respect to the bending, smaller structures such as the metal mesh lines are more susceptible. Such mechanical unevenness due to bending of the dielectric substrate can be mitigated by fabrication processing or choosing more rigid materials. In addition, combined with the dielectric constant deviation, the dielectric loss of the substrate, the loss of the connector and the reduced matching efficiency at the interface caused by welding, the coupling amplitude difference is inevitable. Despite the differences, they do not alter the essence of topological edge states phenomena. It is believed in potential applications such as circuits integration, the differences can be better controlled or pre-adjusted through design iterations and fabrication processing.

IV. DESIGN OF TOPOLOGICAL DIRECTIONAL COUPLERS FOR TERAHERTZ APPLICATIONS

Because of their high robustness and immunity to defects, topological devices have broad application prospects in both millimeter-wave and terahertz systems. The topological waveguides and directional couplers proposed above could be extended to millimeter-wave and terahertz on-chip systems.

To demonstrate that the above design method for topological couplers is applicable to terahertz band, a new topological directional coupler working in a terahertz band around 140 GHz is designed by simply changing the substrate material and structure size as shown in Fig. 6(a), where the dielectric substrate is changed to a 0.1 mm thick quartz with a relative permittivity $\varepsilon = 3.75$ and a loss tangent $\tan\delta$ of 0.00035 whereas the unit cell parameter a is changed to 0.7 mm and $l1 = a$, $l2 = 0.5a$. Fig. 6(b) shows the simulation results of the terahertz topological directional coupler, in which the simulation settings are the same as those in the microwave frequency band studied above. The pass-through, coupling and transmission coefficients of the terahertz topological directional coupler are also comparable with the coupler operated at the microwave band e.g., a -5 dB coupling coefficient could readily be achieved at terahertz frequencies. These results demonstrate that the proposed topological coupler is promising to be applied in both terahertz and millimeter-wave systems.

V. CONCLUSION

In summary, we have proposed the design of topological directional couplers based on planar valley PTIs. The topological directional couplers can be efficiently fed by the conventional microstrip lines and in our experiments, coupling coefficients of -3.5 dB, -5 dB and -7 dB were achieved by simply replacing a few unit cells of the waveguide structure, where the results of simulations and experiments agree well with each other at the microwave band. The reported devices possess superior coupling coefficients and configurability compared with literature [24], [25]. Also, they are better at handling defects or disorder compared with more conventional couplers, such as microstrip directional couplers or waveguide directional couplers. The structure of the designed topological directional coupler is simple and by adjusting its dielectric substrate and structural parameters, the topological directional coupler could work both in microwave and terahertz bands, which holds great promise for future hybrid classical and topological on-chip applications.

REFERENCES

[1] S. K. Ma and S. M. Anlage, "Microwave applications of photonic topological insulators," *Appl. Phys. Lett.*, vol. 116, no. 25, Jun. 2020, Art. no. 250502.

[2] Y. Wu, C. Li, X. Y. Hu, Y. T. Ao, Y. F. Zhao, and Q. H. Gong, "Applications of topological photonics in integrated photonic devices," *Adv. Opt. Mater.*, vol. 5, no. 18, Sep. 2017, Art. no. 1700357.

[3] Y. H. Yang et al., "Terahertz topological photonics for on-chip communication," *Nature Photon.*, vol. 14, no. 7, pp. 446–451, Jul. 2020.

[4] B. L. Li et al., "Valley topological line-defects for Terahertz waveguides and power divider," *Opt. Mater.*, vol. 126, Apr. 2022, Art. no. 112152.

[5] J. Webber et al., "Terahertz band communications with topological valley photonic crystal waveguide," *J. Lightw. Technol.*, vol. 39, no. 24, pp. 7609–7620, Dec. 2021.

[6] W. S. Ruan, X. T. He, F. L. Zhao, and J. W. Dong, "Analysis of unidirectional coupling in topological valley photonic crystal waveguides," *J. Lightw. Technol.*, vol. 39, no. 4, pp. 889–895, Feb. 2021.

[7] D. J. Bisharat and D. F. Sievenpiper, "Electromagnetic-dual metasurfaces for topological states along a 1D interface," *Laser Photon. Rev.*, vol. 13, no. 10, Oct. 2019, Art. no. 1900126.

[8] M. L. N. Chen, L. J. Jiang, Z. Lan, and W. E. I. Sha, "Pseudospin-polarized topological line defects in dielectric photonic crystals," *IEEE Trans. Antennas Propag.*, vol. 68, no. 1, pp. 609–613, Jan. 2020.

[9] M. L. L. N. Chen, L. Jiang, Z. H. Lan, and W. E. I. Sha, "Coexistence of pseudospin- and valley-Hall-like edge states in a photonic crystal with C-3v symmetry," *Phys. Rev. Res.*, vol. 2, no. 4, Oct. 2020, Art. no. 043148.

[10] L. H. Wu and X. Hu, "Scheme for achieving a topological photonic crystal by using dielectric material," *Phys. Rev. Lett.*, vol. 114, no. 22, Jun. 2015, Art. no. 223901.

[11] W. J. Chen et al., "Experimental realization of photonic topological insulator in a uniaxial metacrystal waveguide," *Nature Commun.*, vol. 5, Dec. 2014, Art. no. 5782.

[12] S. Barik, H. Miyake, W. DeGottardi, E. Waks, and M. Hafezi, "Two-dimensionally confined topological edge states in photonic crystals," *New J. Phys.*, vol. 18, Nov. 2016, Art. no. 113013.

[13] Q. L. Chen et al., "Valley-Hall photonic topological insulators with dual-band kink states," *Adv. Opt. Mater.*, vol. 7, no. 15, Aug. 2019, Art. no. 1900036.

[14] J. W. Dong, X. D. Chen, H. Y. Zhu, Y. Wang, and X. Zhang, "Valley photonic crystals for control of spin and topology," *Nature Mater.*, vol. 16, no. 3, pp. 298–302, Mar. 2017.

[15] F. Gao et al., "Topologically protected refraction of robust kink states in valley photonic crystals," *Nature Phys.*, vol. 14, no. 2, pp. 140–144, Feb. 2018.

[16] T. Ma and G. Shvets, "All-Si valley-Hall photonic topological insulator," *New J. Phys.*, vol. 18, Feb. 2016, Art. no. 025012.

[17] D. Xiao, W. Yao, and Q. Niu, "Valley-contrasting physics in graphene: Magnetic moment and topological transport," *Phys. Rev. Lett.*, vol. 99, no. 23, Dec. 2007, Art. no. 236809.

[18] X. X. Wu et al., "Direct observation of valley-polarized topological edge states in designer surface plasmon crystals," *Nature Commun.*, vol. 8, Nov. 2017, Art. no. 1304.

[19] Y. Meng et al., "Non-Hermitian topological coupler for elastic waves," *Sci. China Phys., Mechanics Astron.*, vol. 65, no. 2, Feb. 2022, Art. no. 224611.

[20] X. J. Cheng, C. Jouvaud, X. Ni, S. H. Mousavi, A. Z. Genack, and A. B. Khanikaev, "Robust reconfigurable electromagnetic pathways within a photonic topological insulator," *Nature Mater.*, vol. 15, no. 5, pp. 542–548, May 2016.

[21] Y. T. Ao, X. Y. Hu, C. Li, Y. L. You, and Q. H. Gong, "Topological properties of coupled resonator array based on accurate band structure," *Phys. Rev. Mater.*, vol. 2, no. 10, Oct. 2018, Art. no. 105201.

[22] L. Chen, M. Y. Zhao, H. Ye, Z. H. Hang, Y. Li, and Z. Z. Cao, "Efficient light coupling between conventional silicon photonic waveguides and quantum valley-Hall topological interfaces," *Opt. Exp.*, vol. 30, no. 2, pp. 2517–2527, Jan. 2022.

[23] X. T. He et al., "A silicon-on-insulator slab for topological valley transport," *Nature Commun.*, vol. 10, Feb. 2019, Art. no. 872.

[24] R. J. Davis, D. J. Bisharat, and D. F. Sievenpiper, "Classical-to-topological transmission line couplers," *Appl. Phys. Lett.*, vol. 118, no. 13, Mar. 2021, Art. no. 131102.

[25] G. G. Gentili, G. Pelosi, F. S. Piccioli, and S. Selleri, "Towards topological protection based millimeter wave devices," *Phys. Rev. B*, vol. 100, no. 12, Sep. 2019, Art. no. 125108.

[26] J. W. Holloway, L. Boglione, T. M. Hancock, and R. Han, "A fully integrated broadband sub-mmwave chip-to-chip interconnect," *IEEE Trans. Microw. Theory Tech.*, vol. 65, no. 7, pp. 2373–2386, Jul. 2017.

[27] M. Gao, S. Q. Wu, and J. Mei, "Acoustic topological devices based on emulating and multiplexing of pseudospin and valley indices," *New J. Phys.*, vol. 22, no. 1, Jan. 2020, Art. no. 013016.

[28] C. McDonnell, J. H. Deng, S. Sideris, T. Ellenbogen, and G. X. Li, "Functional THz emitters based on Pancharatnam-Berry phase nonlinear metasurfaces," *Nature Commun.*, vol. 12, no. 1, Jan. 2021, Art. no. 30.

[29] A. Zdagkas et al., "Observation of toroidal pulses of light," *Nature Photon.*, vol. 16, no. 7, pp. 523–528, Jul. 2022.

[30] M. L. Tseng et al., "Vacuum ultraviolet nonlinear metalens," *Sci. Adv.*, vol. 8, no. 16, Apr. 2022, Art. no. eabn5644.

[31] Z. Lan, M. L. N. Chen, F. Gao, S. Zhang, and W. E. I. Sha, "A brief review of topological photonics in one, two, and three dimensions," *Rev. Phys.*, vol. 9, Dec. 2022, Art. no. 100076.